Obstacle-shape effect in a two-dimensional granular silo flow field

K. Endo,[1] K. Anki Reddy,[2] and H. Katsuragi[1]

[1]*Department of Earth and Environmental Sciences, Nagoya University, Nagoya 464-8601, Japan*
[2]*Department of Chemical Engineering, Indian Institute of Technology Guwahati, Guwahati 781039, India*

We conduct a simple experiment and numerical simulation of two-dimensional granular discharge flow driven by gravity under the influence of an obstacle. According to previous work [Zuriguel *et al.*, Phys. Rev. Lett. **107**, 278001 (2011)], the clogging of granular discharge flow can be suppressed by putting a circular obstacle at a proper position. In order to investigate the details of the obstacle effect in granular flow, we focus on particle dynamics in this study. From the experimental and numerical data, we find that the obstacle remarkably affects the horizontal-velocity distribution and packing fraction in the vicinity of the exit. In addition to the circular obstacle, we utilize triangular, inverted-triangular, and horizontal-bar obstacles to discuss the obstacle-shape effect in granular discharge flow. Based on the investigation of dynamical quantities such as velocity distributions, granular temperature, and volume fraction, we find that the triangular obstacle or horizontal bar could be very effective in preventing the clogging. From the result obtained, we consider that the detouring of particles around the obstacle and resultant low packing fraction at the exit region effectively prevent the clogging in a certain class of granular discharge flow.

I. INTRODUCTION

Gravity-driven granular silo flow shows some intriguing phenomena. Its behavior is quite different from usual fluid behavior. For instance, the discharge flow rate of gravity-driven granular silo flow is independent of its height (thickness) in the silo. Such a constant flow cannot be achieved when usual fluid is used. In usual fluid, the discharge flow rate varies depending on the layer's height (Torricelli's theorem [1]). The pressure structure within a granular silo tends to saturate in the deep part due to the Janssen effect [2]. This saturated (constant) pressure could be a reason for the constant flow rate. However, according to the study in [3], the constant granular flow might not be related to the Janssen effect. Namely, the origin of steadiness in granular silo flow is not yet fully understood. Beverloo *et al.* experimentally obtained the scaling for the flow rate in granular silo flow, which depends on the sizes of particles and exit [4]. In particular, when the exit width W decreases to a certain limit (e.g., $W \simeq 6D$, where D is the particle diameter), an arched structure of granular particles could easily be formed around the exit [5]. Due to this arch formation, particles suddenly clog to arrest the flow [6–9]. The clogging phenomenon is often a severe problem in transporting granular materials in industry.

An obstacle placed within the granular silo flow could affect a flow property such as the clogging condition. In fact, the clogging probability is decreased by inserting an obstacle into the granular silo at the proper position [10–12]. The clogging phenomena have also been observed in crowd and animal flows, and obstacles have been used to control these flows as well [13–15]. By the experimental simulation of evacuating exit flow, it has been revealed that the obstacle set in front of the exit can decrease the outflow period [12,16]. Although the vibration or concentrated air flow can also be utilized to avoid the granular clogging [8,17], obstacle usage is much easier than vibration and air flow in various situations.

Arch formation by particles at the exit region is the fundamental process to proceed to the clogging. The smaller the exit size is, the larger the clogging probability becomes. Recently, nonzero clogging probability even for a very large exit has been proposed on the basis of an experimental result [18]. Self-similar density and velocity profiles around the exit have also been observed [19].
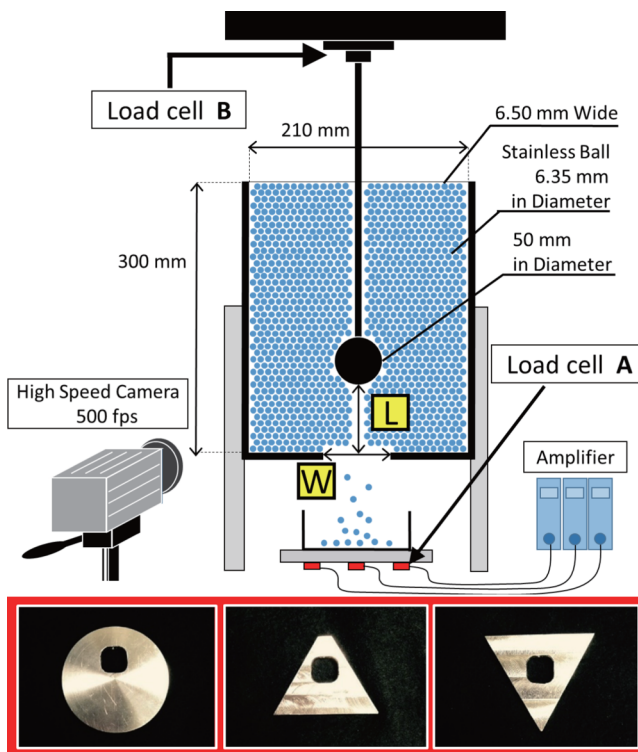
FIG. 1. Experimental apparatus and obstacles. A schematic diagram of the experimental setup is shown above. The width of the exit W and distance between the exit and obstacle L are principal parameters in this system. The lower images show obstacles used in this experiment: a circle 50 mm in diameter, an equilateral triangle with one side 50 mm, and an inverted equilateral triangle with one side 50 mm. Holes in the obstacles were opened to add the attaching mechanism.

In addition, the velocity field in granular silo flow without an obstacle has been studied in various works [20–23]. However, the characteristics of the granular-flow field under the influence of an obstacle is not yet well understood. Moreover, the details of flow-field conditions must be influenced by the shape of the obstacle and/or particles as well. Although the particle-shape dependence of granular silo flow has recently been studied [24], the effect of the shape of the obstacle has not yet been extensively studied.

Therefore, we conducted a simple experiment and numerical simulation of two-dimensional granular silo flow driven by gravity under the influence of an obstacle. In the experiment, we traced individual particles from the flow images acquired by a high-speed camera. Numerical simulation of granular silo flow has also been performed to confirm the major effect of the obstacle to prevent the clogging. In particular, we mainly compare the various obstacle-shape results in order to discuss the physical origin of clogging reduction by the obstacle.

II. METHODS

A. Experiment

An experimental system that we built and pictures of the obstacles used are shown in Fig. 1. In this experiment, we prepare a two-dimensional cell consisting of two acrylic transparent plates and aluminum rectangles for the side and bottom walls. The inner dimension of the cell is

$6.50 \times 210 \times 300$ mm^3 [(thickness) $\times$ (width) $\times$ (height)]. The obstacles are made of stainless steel and are 6.0 mm thick. We use three types of obstacles: a circle 50 mm in diameter, an equilateral triangle with one side 50 mm, and an inverted equilateral triangle of the identical size. After inserting an obstacle and filling the cell with stainless-steel particles (6.35 ± 0.05) mm in diameter, a discharge flow is triggered by opening a small exit at the center of the cell's bottom. We do not refill the container with particles. Namely, the measurement lasts until all the particles are discharged or clogging occurs.

Discharged particles are caught by a container placed below the cell. Load cell sensors (LMB-A, KYOWA) are used to measure the mass of discharged particles. The obstacle is fixed to a stainless-steel pole 6.0 mm in diameter, which is connected to a universal testing machine (AG-X, SHIMADZU) to control the position of the obstacle. Drag force exerted on the obstacle can also be measured using the testing machine. However, here we focus on the clogging problem in this paper. The drag force characterization will be presented elsewhere [25]. Flow rate data are taken at a sample rate of 100 samples/s. We also measure the microscopic granular flow field by using a high-speed camera (FASTCAM SA5, Photron). The acquired images are analyzed by means of a particle tracking velocimetry (PTV) method implemented by LABVIEW software (vision toolkit). The frame rate is fixed at 500 frames/s. The spatial resolution of the images is 0.26 mm/pixel and the images consist of 832×880 pixels corresponding to a field of view of 220×233 mm^2.

The main parameters in this experiment are the width of the exit W and the vertical distance between the exit and obstacle L. Specifically, W is varied as 25, 30, 40, and 60 mm; L is changed by 5 mm from $L = 0$ mm to $L = 50$ mm and by 10 mm from $L = 50$ mm to $L = 100$ mm. The case without any obstacle is denoted by $L = \infty$.

B. Simulation methodology

We used the contact force models based on [26] and explained further in [27] to simulate the gravity-driven flow of granular media. Supposing that a particle i is in contact with particle j, the contact force on particle i resolved into two components (along the line joining centers and perpendicular to the line joining centers) can be expressed as $\mathbf{F}_{ij} = \mathbf{F}_{ij}^n + \mathbf{F}_{ij}^t$. For the present model, the normal and tangential force components are given by $\mathbf{F}_{ij}^n = \sqrt{\delta_{ij}}\sqrt{\frac{R_i R_j}{R_i + R_j}}(k_n \delta_{ij}\mathbf{n}_{ij} - m_{\text{eff}}\gamma_n \mathbf{v}_{ij}^n)$ and $\mathbf{F}_{ij}^t = \sqrt{\delta_{ij}}\sqrt{\frac{R_i R_j}{R_i + R_j}}(k_t \mathbf{u}_{ij}^t - m_{\text{eff}}\gamma_t \mathbf{v}_{ij}^t)$, respectively. Here R_i and R_j are the radii of particles i and j. If particle i and particle j respectively have positions $\mathbf{r}_i$ and $\mathbf{r}_j$, masses m_i and m_j, linear velocities $\mathbf{v}_i$ and $\mathbf{v}_j$, and angular velocities $\mathbf{w}_i$ and $\mathbf{w}_j$, the quantities used in the above force equation are defined as $\delta_{ij} = d - |\mathbf{r}_i - \mathbf{r}_j|$, $\mathbf{v}_{ij}^n = (\mathbf{v}_{ij} \cdot \mathbf{n}_{ij})\mathbf{n}_{ij}$, $\mathbf{v}_{ij} = \mathbf{v}_i - \mathbf{v}_j$, $\mathbf{v}_{ij}^t = \mathbf{v}_{ij} - \mathbf{v}_{ij}^n - \frac{1}{2}\mathbf{r}_{ij} \times (\mathbf{w}_i + \mathbf{w}_j)$, $\mathbf{n}_{ij} = \mathbf{r}_{ij}/|\mathbf{r}_{ij}|$, and $m_{\text{eff}} = m_i m_j/(m_i + m_j)$.

Once the force acting on particle i is known, classical equations of motion can be integrated with the suitable numerical technique to update its position and velocities. In the simulation, the elastic constant for normal contact k_n is $2 \times 10^8 mg/d^2$, whereas the elastic constant in the tangential direction k_t is $\frac{2}{7}k_n$ [27–29]. Here m is the mass and d is the diameter of the particle and g is the acceleration due to gravity. The viscoelastic damping constant for normal contact γ_n is $1850\sqrt{g}/d^{1.5}$ and for tangential contact γ_t is half of the γ_n. The chosen constants represent the properties of material used in the experimental study. It is important to mention that we include memory effect in the modeling of tangential forces. Tangential displacement between the two contact particles $\mathbf{u}_{ij}^t$ will be computed from the initiation of the contact (it will be zero at the initiation of contact) and it is adjusted so that the local yield criterion $|\mathbf{F}_{ij}^t| < |\mu \mathbf{F}_{ij}^n|$ is satisfied. The rate of change of this elastic tangential displacement $\mathbf{u}_{ij}^t$ is given by $d\mathbf{u}_{ij}^t/dt = \mathbf{v}_{ij}^t - (\mathbf{u}_{ij}^t \cdot \mathbf{v}_{ij})\mathbf{r}_{ij}/|\mathbf{r}_{ij}|^2$. In the present simulations, the friction coefficient μ has been set equal to 0.36 for particle-particle interactions (based on the angle of repose value for stainless-steel spheres). In the literature it is reported that for a combination of mild steel and aluminum μ is 0.42 and for aluminum brass and mild steel it is
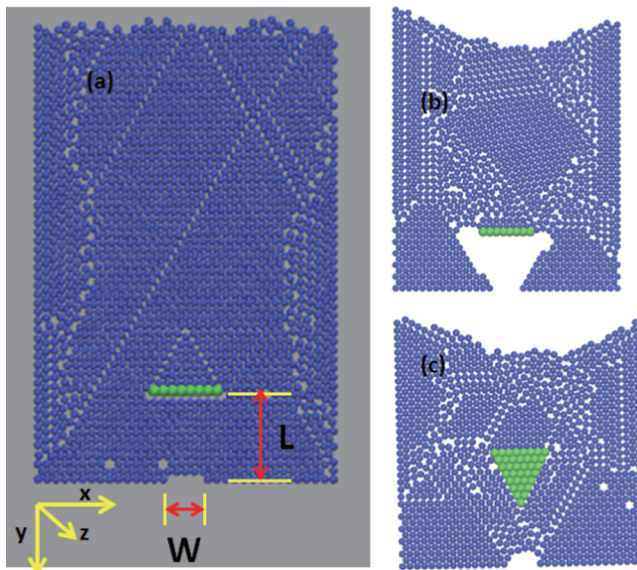
FIG. 2. (a) Simulation system with a horizontal-bar obstacle consisting of green spheres. Typical clogging configurations were observed in simulations for (b) the flow past the horizontal-bar obstacle, with $L = 45$ and $W = 25$ mm, and (c) the flow past the inverted-triangle obstacle, with $L = 60$ and $W = 25$ mm.

0.6 [30]. In the simulations we used 0.5 to represent the static friction coefficient for the particle-wall interaction (wall is made of aluminum in our experiments). The time step in the present simulation is 0.000 002. We arrived at this value of time step by computing the collision time with the help of equations given in [26,31] and this collision time was found to be $O(10^{-4})$. All the lengths are scaled by particle diameter d, which is 1.0 in the present case. Time, velocities, and forces are measured in units of $\sqrt{d/g}$, $\sqrt{gd}$, and mg, respectively. Elastic constants and viscoelastic damping constants are measured in units of mg/d^2 and $\frac{1}{\text{(time)} \times \text{(distance)}}$. The density of the particles is also set equal to 1.0. The obstacle shape in the present simulation is made using spherical particles of diameter 1.0. For example, to create a circular obstacle of diameter $8d$, we need approximately 22 particles to make the outer layer of a circle. Similarly, to make a triangular obstacle with a side of length of $8d$, we need 36 particles.

The initial configuration is prepared by pouring the particles into a container under gravity. There are 1900 particles in the simulation, which is in correspondence with the number of particles used in experimental study discussed in this paper. The dimensions of the simulation box are $34d \times 48d \times 1d$. The simulation system is as shown in Fig. 2. Flat frictional walls are present in the x direction and periodic boundary conditions are applied in the z direction. The bottom wall in the y direction is made up of spherical particles $1.0d$ in diameter and to simulate the discharge of particles through orifice, a certain number of spheres will be removed from the bottom y wall (for $W = 25$ mm, we need to remove four spheres from the bottom wall). All the simulations are carried out using a large-scale atomic/molecular massively parallel simulator [32]. In the experiment, the mean grain diameter is 6.35 mm. To make a comparison between the numerical and experimental data, L and W values in the simulation are transformed to the real length scale by multiplying the grain diameter by 6.35 mm in the following data plots. Furthermore, the elastic constant for normal contact used in the simulation results in a Young modulus Y of 108.5 GPa for a stainless-steel spherical particle of diameter 6.35 mm if we use the equation $k_n = \frac{2Y}{3(1-\nu^2)}$. Here the density and Poisson's ratio ν for stainless steel are taken as 8000 kg/m^3 and 0.275, respectively. These values are more or less reasonable for steel.
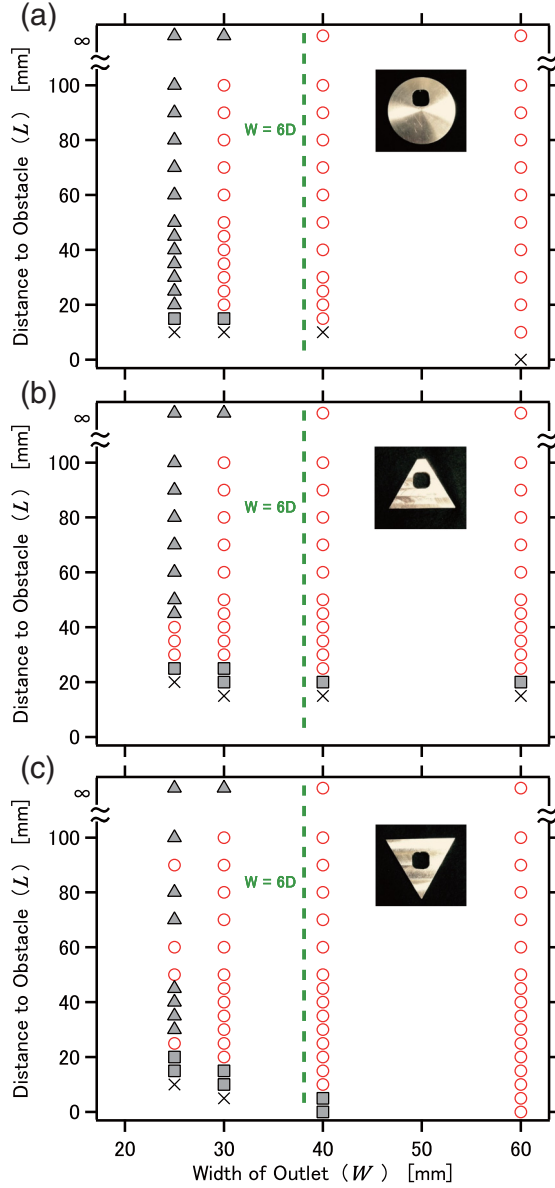
FIG. 3. Clogging diagrams for (a) circular, (b) triangular, and (c) inverted-triangular obstacle cases. Experiments were conducted three or more times (in $W \leqslant 40$ mm) to make this diagram. Here $L = \infty$ means the case without an obstacle. Circles indicate that the clogging did not occur. Triangles indicate that the clogging by arching at the exit [Fig. 4(a)] occurred. Squares indicate that the clogging occurred between the obstacle and the bottom wall [Fig. 4(b)]. Crosses indicate that granular flow did not occur at all. Green dashed line corresponds to $W = 6D$.

III. EXPERIMENTAL RESULTS AND ANALYSIS

A. Clogging diagram

First, the clogging-occurrence conditions depending on W and L are examined. Figure 3 shows the clogging diagrams obtained for circular [Fig. 3(a)], triangular [Fig. 3(b)], and inverted-triangular
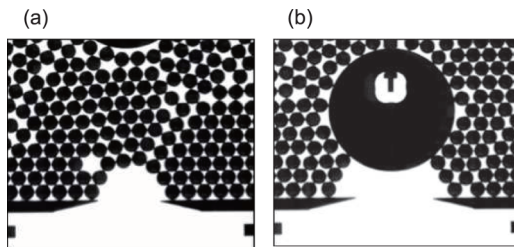
FIG. 4. (a) Clogging by the arch formation (a) around the exit and (b) between the obstacle and bottom wall.

[Fig. 3(c)] cases. Three or more experimental runs are performed for each experimental condition. If the flow clogs during discharge at least once, that condition is regarded as a clogging case. On the other hand, if all the particles are discharged without clogging for all experimental runs, that condition is assigned to the no-clogging case. In Fig. 3, no clogging is expressed by circles, while triangles, squares, and crosses indicate the clogging conditions. In this study, the number of experimental runs might not be sufficient to precisely discuss the clogging probability. Moreover, we did not compute the avalanche size distribution. Thus, the clogging diagrams shown in Fig. 3 are more or less qualitative ones. Therefore, a quantitative analysis for the clogging probability will not be discussed in this study. However, some characteristic features can be confirmed in these diagrams, as discussed below.

As shown in Figs. 2(c) and 4(a), the clogging is basically induced by an arched structure formed at the exit region. If an obstacle is too close to the exit (i.e., L is too small), arch formation occurs between the obstacle and bottom wall [Fig. 4(b)]. This type of arch formation is different from the ordinary one that is formed around the exit [Fig. 4(a)]. In the clogging diagram (Fig. 3), the arch formation around the exit is denoted by triangles and the arch formation between the obstacle and bottom wall is presented by squares. If the flow is not induced from the very initial state, crosses are assigned. In the numerical simulation, a slightly different clogging mode [Fig. 2(b)] is also observed. In this clogging mode, the arch is formed around the obstacle edge and the stable triangular lattice slope. Although this could be regarded as a type of obstacle-wall clogging, this mode cannot be observed in the experiment since it is difficult to make the stable triangular lattice slope in the actual experiment.

When W is large enough, the flow is relatively smooth and difficult to clog. By contrast, when $W = 25$ mm, clogging frequently occurs. In Fig. 3(a) (circular-obstacle case), the L dependence of the clogging occurrence is not clear. In Fig. 3(c) (inverted-triangular-obstacle case), although some no-clogging states can be found in $W = 25$ mm, any clear trend of L-dependent clogging occurrence cannot be confirmed. In contrast, in Fig. 3(b) (triangular-obstacle case), a clear reduction of the clogging occurrence can be confirmed in the relatively small L regime ($30 \, \mathrm{mm} \leqslant L \leqslant 40 \, \mathrm{mm}$). This anticlogging tendency due to the obstacle is qualitatively consistent with the previous work using a circular obstacle [10]. In this study, the anticlogging by placing an obstacle can clearly be confirmed, particularly in the triangle case.

From the above-mentioned observations, we consider that the flow situation could significantly depend on the shape of the obstacle. At $W = 30$ mm, clogging due to the arch formation at the exit region occurs only at $L = \infty$ (no-obstacle case). The case of $W = 25$ mm is more interesting because the clogging occurrence variation depending on L can be observed. The condition to prevent the clogging might be revealed by comparing these cases (no obstacle, circular obstacle, triangular obstacle, and inverted triangular obstacle) at $W = 25$ mm. Therefore, we focus on the case of $W = 25$ mm in the following.

B. Granular flow field

In this study, we would like to relate macroscopic behaviors of granular discharge flow to the statistics of motion of individual particles. Thus, we track particle motion using PTV method.

The examples of velocity fields computed from the series of images of flowing particles acquired by a high-speed camera are shown in Fig. 5. Figures 5(a) and 5(b) show the case with no obstacle, Figs. 5(c) and 5(d) the case with a circular obstacle, Figs. 5(e) and 5(f) the case with a triangular obstacle, and Figs. 5(g) and 5(h) the case with an inverted triangular obstacle. Experimental conditions in these data are $W = 25$ mm and $L = 30$ mm, at which the flow is in the marginal state between smooth flow and clogging. Each case has a snapshot of the raw particle image in Figs. 5(a), 5(c), 5(e), and 5(g) and the corresponding velocity field in vector representation is shown in Figs. 5(b), 5(d), 5(f), and 5(h).

We first discuss on the no-obstacle case. In Fig. 5(b), we can confirm that the vertical component dominates the particle velocities. The relatively-high-speed particles are distributed at the central zone of the cell (right above the exit). The meandering of flow in this state might be related to the local crystallization due to the monodispersity of particles. Although this velocity field results in the high flow rate, dense flow at the exit region might cause clogging due to the arch formation. Indeed, the highest flow rate in no-obstacle case has been confirmed [see the legend in Fig. 7(a)]. It should be noted that all the experiments show steady flow [25,33] even right before the clogging. Although some numerical simulations have reported an increase of the flow rate as a result of the obstacle [34,35], these studies have simulated the inclined-bottom-wall silo flow. Furthermore, [35] has used the fluctuation of grains and vibration of walls to prevent the clogging. This could significantly affect the flow rate as well. Experiments with a horizontal-bottom-wall silo have also shown a similar increase of flow rate as a result of the obstacle [11]. However, its trend of an increasing flow rate was not very significant.

Next, let us focus on the circular-obstacle case. In Figs. 5(c) and 5(d), the particle configuration and corresponding velocity field of granular flow with a circular obstacle are presented. As can be seen in Fig. 5(c), more structural defects in the particle configuration are introduced (compared to the no-obstacle case) due to the presence of a large circular obstacle. In addition, the velocity field in this case becomes asymmetric as shown in Fig. 5(d). At this moment, particles in the left region are much more active than on the other side. Actually, this asymmetry results in the temporal oscillation of the active zone, i.e., the alternate flow is developed. Namely, the obstacle triggers the spatiotemporal inhomogeneity in the granular discharge flow. This inhomogeneity could be a possible reason to avoid the clogging. However, as shown in the clogging diagram [Fig. 3(a)], the relation between the clogging and the circular obstacle is not so clear. Moreover, we have confirmed that the discharge flow rate is almost always steady even in the alternate flow regime [33].

The effect of the obstacle is exaggerated by using a triangular obstacle. In Figs. 5(e) and 5(f), the particle configuration and corresponding velocity field with a triangular obstacle are shown. Qualitative characteristics observed in Figs. 5(e) and 5(f) are more or less similar to those seen in Figs. 5(c) and 5(d). Spatiotemporal inhomogeneity including alternate flow can be induced in this case as well. Moreover, the particle-number density (packing fraction) beneath the obstacle (above the exit) significantly decreases in Figs. 5(e) and 5(f). Since the clogging prevention by the obstacle is most significant in this triangular case, an essential key effect to prevent the clogging must be present in this triangular-obstacle case. This point will be discussed later from the viewpoint of velocity distribution and packing fraction.

When we use a triangular obstacle fixed upside down (inverted triangle), a different flow field is observed as shown in Figs. 5(g) and 5(h). Since the angle of the triangle is commensurate with the triangular lattice structure, particle configuration shows the crystalline structure even in the region between the obstacle and bottom wall. In addition, the converging flow at the exit region can be observed. The flow field is relatively symmetric compared to the circular and triangular cases, while it still shows a slight asymmetry. Furthermore, the packing fraction right above the exit is not reduced very much in this case.
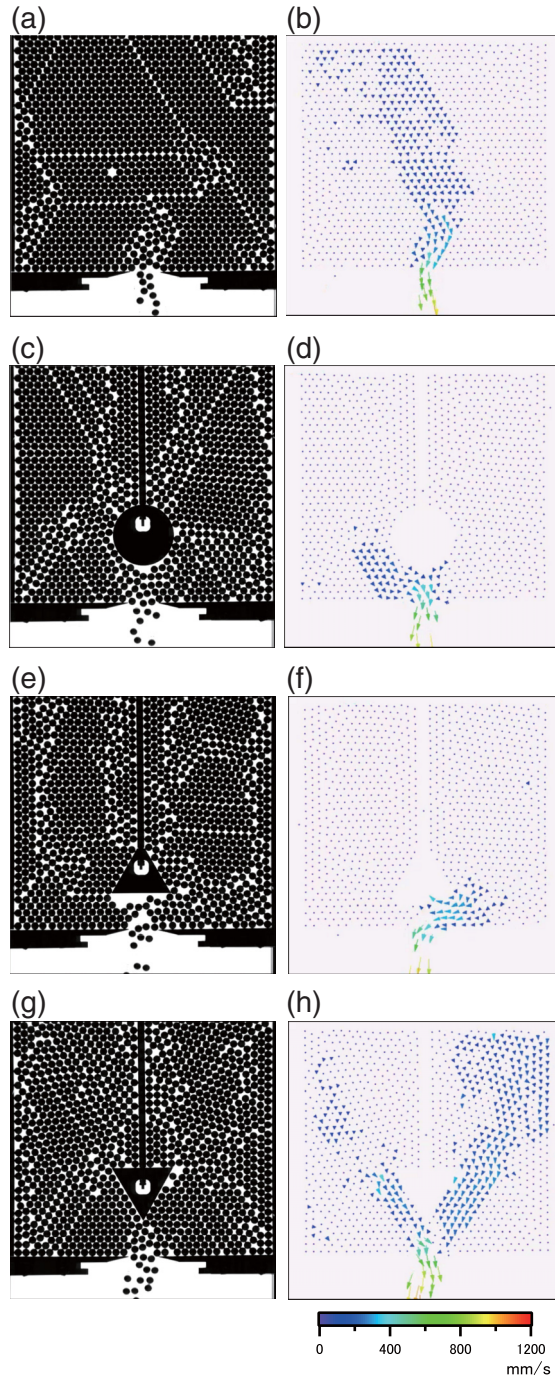
FIG. 5. Velocity fields of granular discharge flow acquired by a high-speed camera and computed by the PTV method: (a) snapshot of particle configuration without an obstacle, (b) its velocity field computed by each particle's motion in vector representation, (c) snapshot of particle configuration with a circular obstacle, (d) its corresponding velocity field, (e) snapshot of particle configuration with a triangular obstacle, (f) its corresponding velocity field, (g) snapshot of particle configuration with an inverted-triangular obstacle, and (h) its corresponding velocity field. Experimental conditions are fixed at $W = 25$ mm and $L = 30$ mm.
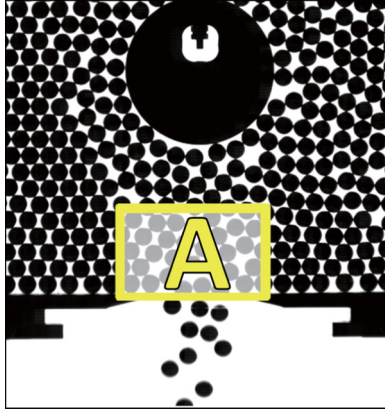
FIG. 6. Definition of the focused region A. The yellow square region (region A) is fixed at the central part above the exit and is 50 mm wide and 30 mm high. When L is smaller than 30 mm, the height is adjusted to the value of L.

C. Analysis of particle motions

In order to discuss the principal effect for avoiding the clog, here we analyze the region above the exit A (the yellow square region shown in Fig. 6). All data shown in this section are based on the analysis in region A. The width and height of region A are basically fixed to 50 mm and 30 mm, respectively. When $L < 30$ mm, however, the height of region A is adjusted to L. With respect to the definition of the spatial axis, the top left corner in the acquired image corresponds to the origin of the vertical (y) and horizontal (x) axes. The positive direction of the y axis is taken to be the gravitational downward direction.

1. Vertical velocity

To characterize the velocity field, its probability density function (PDF) is computed from the PTV data. First, the vertical component V_y is focused. The measured PDF of V_y is shown in Fig. 7(a). In Fig. 7(a), different colors (and line codes) represent the different obstacle shapes. To reveal the effect of obstacle shape, experimental conditions are fixed at $W = 25$ mm and $L = 30$ mm. The qualitative form of the PDF is basically identical among all the data shown in Fig. 7(a). In the large-V_y regime, exponential-like tail can be observed. This part must principally determine the discharge flow rate. Obviously, the velocity level is reduced by the effect of obstacle. In other words, the probability of large V_y in the no-obstacle case is larger than in other obstacle cases. The corresponding flow rates are shown in the legend of Fig. 7(a). This tendency is consistent with the flow rate reduction due to the obstacle effect [25,33]. Note that the discharge flow rate is always steady independently of obstacle shapes [25,33]. In Fig. 7(a), relatively small number of particles have negative V_y. This negative V_y stems from the effective backscattering due to the particle-particle collisions.

2. Horizontal velocity and granular temperature

Next we focus on the behavior of horizontal velocity V_x. Figure 7(b) shows the PDF of V_x at $W = 25$ mm and $L = 30$ mm. These PDFs have a symmetric form because the shape of the obstacle is symmetric. The effect of alternate flow is wiped out by the spatiotemporal average to make the PDF. The width of the PDF depends on the shape of the obstacle. In the excited (dilute) granular gas, the stretched-exponential-type PDF has been observed in many experiments [36–38]. However, here we are not going to examine the detailed structure of the PDF because the statistics to discuss the detailed shape is limited in this experiment. Instead, we simply discuss the global-shape characterization of the PDF. Specifically, the width of the PDF becomes the largest
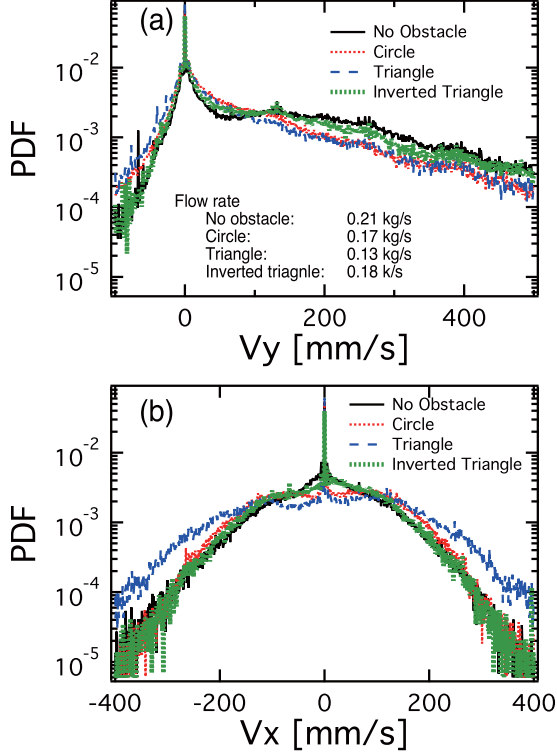
FIG. 7. (a) Vertical velocity distribution in region A. The PDF of V_y at $W = 25$ mm and $L = 30$ mm is shown. The positive direction of V_y corresponds to the gravitational (downward) direction. (b) Horizontal velocity distribution in region A. The PDF of V_x at $W = 25$ mm and $L = 30$ mm is shown.

in the triangular-obstacle case, while others are somewhat similar in the large-$|V_x|$ regime. Also, in the small-$|V_x|$ regime ($|V_x| \leqslant 100$ mm/s), the obstacle dependence in the PDF structure can be observed. The no-obstacle and inverted-triangular-obstacle cases result in qualitatively similar PDF forms in which the population of smaller $|V_x|$ is always larger than that of larger $|V_x|$. On the other hand, the population dips in the relatively-small-$|V_x|$ regime can be confirmed in the cases of circular and triangular obstacles. Sharp peaks confirmed at $V_x \simeq 0$ come from the almost stopping particles in the silo. Similar peaks can also be found in the V_y PDF [Fig. 7(a)].

To characterize the statistical property of V_x, here we introduce the granular temperature in the horizontal direction $T_{gx} \sim \langle \delta V_x^2 \rangle = \langle (V_x - \langle V_x \rangle)^2 \rangle$, where $\langle \cdot \rangle$ indicates the spatiotemporal average. Since this granular temperature corresponds to the variance of the PDF, it can be used to characterize the width of the distribution. The measured T_{gx} as a function of L at $W = 25$ mm is shown in Fig. 8(a). As expected, T_{gx} in the triangular-obstacle case is larger than the other obstacle cases in the small-L regime. The sudden increase of T_{gx} at small L comes from the detouring of particles around the obstacle. The detouring followed by collisions below the obstacle results in the large horizontal velocity component. Note, however, that T_{gx} in the case of a circular obstacle also significantly increases in the very-small-L regime. Since the clear and significant decrease of the clogging occurrence can be detected only for a triangular obstacle in the small-W and -L regime (Fig. 3), it is difficult to explain the anticlogging mechanism solely by large T_{gx}.

3. Packing fraction

Another possible reason for reducing the clogging risk is the low packing fraction ϕ. Here ϕ is defined by the ratio of the particles area relative to the total area in region A. The measured ϕ as
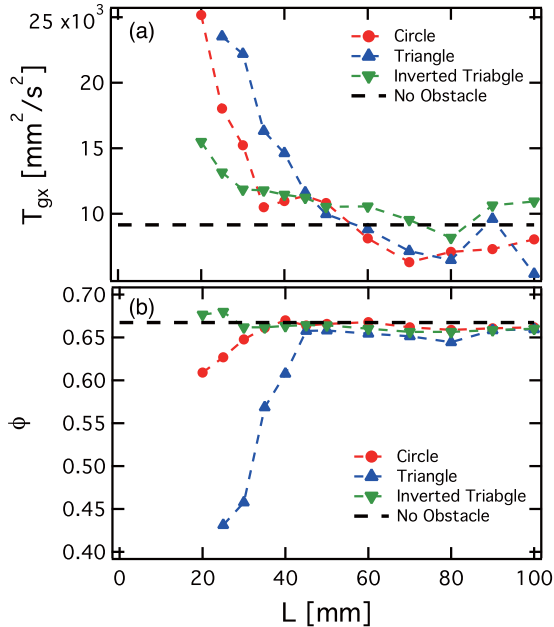
FIG. 8. The L dependence of (a) the horizontal granular temperature T_{gx} and (b) the packing fraction ϕ at $W = 25$ mm. As the obstacle approaches the exit (L becomes small) (a) T_{gx} increases and (b) ϕ decreases. Horizontal dashed lines indicate the levels of the no-obstacle case.

a function of L at $W = 25$ mm is shown in Fig. 8(b). As expected, ϕ decreases as L decreases. Furthermore, the decreasing rate of ϕ is much more significant in the triangular-obstacle case than in the other two cases. This result is consistent with the fact that the triangular-obstacle case shows a clear reduction of clogging occurrence in the small-L and -W regime (Fig. 3). Because the clogging reduction is clearly confirmed in $L < 40$ mm (at $W = 25$ mm) with the triangular obstacle [Fig. 3(b)], we can consider that the sufficiently small ϕ ($\leqslant 0.6$) can safely prevent the clogging in two-dimensional granular flow through a narrow exit. This result is qualitatively consistent with [39]. Obviously, the very small packing fraction is better to prevent clogging. In the very-small-L ($\leqslant 25$ mm) regime, clogging by the arch formation between the obstacle and bottom wall [Fig. 4(b)] is observed. In this regime, ϕ in region A is no longer relevant to discuss the clogging. Rather, the packing fraction in the side regions would be important in this regime. Namely, the important quantity is the packing fraction at the clogging (arch formation) region. In the case of an inverted triangle, ϕ remains large (greater than or equal to 0.65). Nevertheless, the inverted triangle can make smooth flow in some (seemingly random) regimes in the clogging diagram [Fig. 3(c)]. This point will be discussed later.

Finally, we directly compare ϕ with T_{gx} at $W = 25$ mm. We can see the negative correlation between ϕ and T_{gx} in the large-T_{gx} regime (Fig. 9). The decreasing rate of ϕ becomes the maximum in the triangular case. This means that the triangular shape is the most efficient one to reduce ϕ by the identical T_{gx}. The flat bottom of the obstacle could play a crucial role in achieving this efficiency. To investigate the details of this shape dependence, force visualization by photoelastic material [40–43] and/or numerical simulation [44] might be helpful. In this study, we perform the numerical simulation as presented below.

IV. NUMERICAL RESULTS AND ANALYSIS

Next we compare the numerical result with experiment. In Fig. 10, the numerically obtained PDF of V_y and V_x, the horizontal granular temperature T_{gx}, and the packing fraction ϕ are shown.
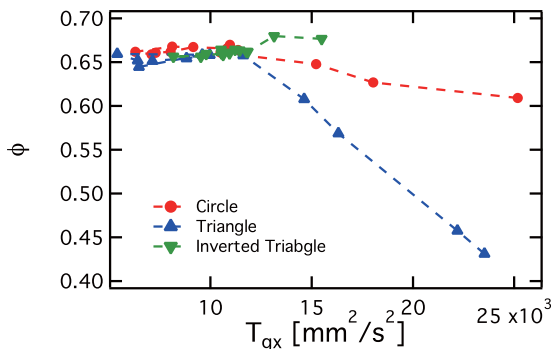
FIG. 9. Correlation between packing fraction ϕ and horizontal granular temperature T_{gx} at $W = 25$ mm.

The parameter values of W and L used here are the same as those used in the experiment. From the experimental observation, we guess that the particles detouring due to the obstacle and the horizontal bottom shape are the principal factors to make small ϕ. Thus, in the numerical simulation, we employ a horizontal-bar obstacle instead of the triangle. We also examine the cases with circular and inverted-triangular obstacles. As can be seen in Fig. 10, almost all qualitative characteristics observed in the experiment are reproduced by the numerical simulation. Then the horizontal bar in the numerical simulation should correspond to the triangle in the experiment. Although the PDF shapes of V_y and V_x are slightly different from experimentally obtained ones, the obstacle-shape dependence of the PDF shape and L dependences of T_{gx} and ϕ are basically captured by the numerical result. This result supports our speculation: Particles detouring around the obstacle and horizontal bottom shape of the obstacle significantly reduce ϕ below the obstacle (at the exit region). In addition, the reduced ϕ decreases the clogging risk (and flow rate).

V. DISCUSSION

From the above observations, we suppose that the principal effect induced by the obstacle in the granular discharge flow field is as follows. By the presence of an obstacle in the vicinity of the exit, particles have to detour to approach the exit. Thereby, the particle-supply rate to the exit region is decreased by the detouring effect. This effect directly reduces the local packing fraction at the exit region. The most significant detouring can be made by the triangular obstacle (or horizontal bar). In addition, at the central part beneath the obstacle, strong collisions occur among the particles coming from the left and right sides. Then the random motion of particles, which corresponds to the temperature in this system (granular temperature), is increased. Finally, the packing fraction right above the exit is further reduced by the excluded-volume effect of active (high-temperature) particles. As a consequence, the resultant low packing fraction prevents the arch formation at the exit. Thus, these obstacle effects can avoid the clogging occurrence. In this sense, the obstacle is useful in preventing the clogging by making small ϕ.

This simple scenario to prevent the clogging cannot explain all the situations. For instance, when the inverted-triangular obstacle is used, the clogging can be observed rather randomly at $W = 25$ mm [Fig. 3(c)] in spite of large ϕ. This result implies that the clogging prevention can be achieved even in the large-ϕ regime. We speculate that the crystal-like ordered structure made in the exit region could be a key to keep large ϕ by the inverted triangle [Fig. 5(g)]. Although such an ordered structure yields the large ϕ, its structure could flow systematically, forming a cluster without developing an arch, as long as it does not create the obstacle-wall arch like in Fig. 2(b). Then the competition between high density and clustering might result in a very stochastic (not systematic) clogging as observed in the inverted-triangular case at $W = 25$ mm. Moreover, the pressure decrease above the obstacle
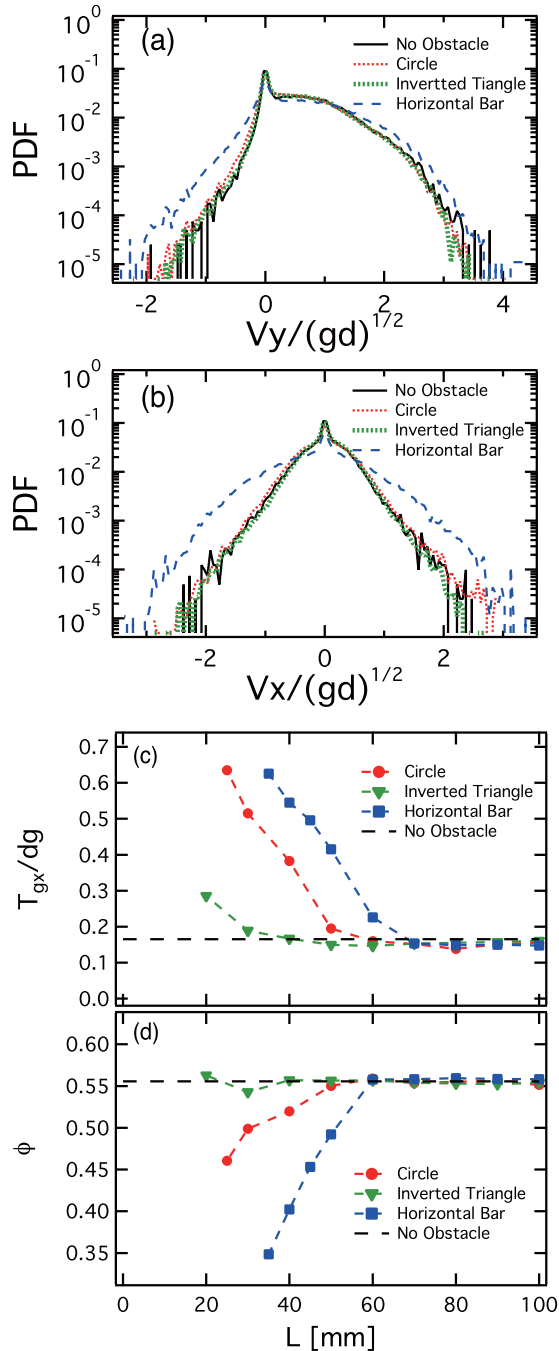
FIG. 10. Numerically obtained data of (a) the vertical velocity PDF, (b) the horizontal velocity PDF, (c) the horizontal granular temperature, and (d) the packing fraction. For (a) and (b), parameters are $W = 25$ mm and $L = 50$ mm, and for (c) and (d), $W = 25$ mm.

will also be effective in preventing the clogging [10]. Namely, there might be plural mechanisms to prevent the clogging by the obstacle. Detail classification and characterization of various obstacle effects are still important problems left for future study.

There are some interesting issues we have not discussed in this paper. For example, spatiotemporal analyses of alternate flow typically observed in circular- and triangular-obstacle cases have not been performed. Actually, the experimental conditions to reproduce the alternate flow could not be precisely determined from our experimental result. It occurred rather in a random fashion. Perhaps its classification might be more complex than making the clogging diagram. In addition, the preliminary measured switching period of the alternate flow also seemed to be neither universal nor systematic. Its characterization is one of the challenging issues open to future study. In addition, the forms of the PDF (Fig. 7) have not been discussed in detail. Only T_{gx} has been used in this study. Its detail characterization is also an interesting problem left to future investigation.

VI. CONCLUSION

We conducted a simple experiment and numerical simulation of two-dimensional granular flow driven by gravity under the influence of an obstacle. From the images of the granular exit flow acquired by a high-speed camera, we tracked the motion of individual particles at the exit region by means of the PTV method. By the triangular obstacle, the clogging occurrence can be reduced at a certain distance range from the exit. The principal reason for this clogging prevention is the low packing fraction in the vicinity of exit. The free space among the particles seems to be effectively created when the triangular obstacle approaches the exit. At the same time, the triangular obstacle also results in the large granular temperature in the horizontal direction. The detouring by the triangle can decrease the supply of the particles to the exit region and also activate the particles by collisions to have a high-velocity component in the horizontal direction. These behaviors were reproduced by the numerical simulation as well. In addition, the numerical simulation also revealed that the horizontal bar is enough to create the above-mentioned situation: small ϕ below the obstacle (above the exit region).

ACKNOWLEDGMENTS

---

[1] T. E. Faber, *Fluid Dynamics for Physicists* (Cambridge University Press, Cambridge, 1995).

[2] H. A. Janssen, Versuche über getreidedruck in silozellen, Z. Ver. Dt. Ing. **39**, 1045 (1895), (in German).

[3] M. A. Aguirre, J. G. Grande, A. Calvo, L. A. Pugnaloni, and J. C. Géminard, Pressure Independence of Granular Flow through an Aperture, Phys. Rev. Lett. **104**, 238002 (2010).

[4] W. A. Beverloo, H. A. Leniger, and J. van de Velde, The flow of granular solids through orifices, Chem. Eng. Sci. **15**, 260 (1961).

[5] D. Helbing, A. Johansson, J. Mathiesen, M. H. Jensen, and A. Hansen, Analytical Approach to Continuous and Intermittent Bottleneck Flows, Phys. Rev. Lett. **97**, 168001 (2006).

[6] K. To, P.-Y. Lai, and H. K. Pak, Jamming of Granular Flow in a Two-Dimensional Hopper, Phys. Rev. Lett. **86**, 71 (2001).

[7] K. To, Jamming transition in two-dimensional hoppers and silos, Phys. Rev. E **71**, 060301 (2005).

[8] I. Zuriguel, A. Garcimartín, D. Maza, L. A. Pugnaloni, and J. M. Pastor, Jamming during the discharge of granular matter from a silo, Phys. Rev. E **71**, 051303 (2005).

[9] A. Janda, I. Zuriguel, A. Garcimartín, L. A. Pugnaloni, and D. Maza, Jamming and critical outlet size in the discharge of a two-dimensional silo, Europhys. Lett. **84**, 44002 (2008).

[10] I. Zuriguel, A. Janda, A. Garcimartín, C. Lozano, R. Arévalo, and D. Maza, Silo Clogging Reduction by the Presence of an Obstacle, Phys. Rev. Lett. **107**, 278001 (2011).

[11] C. Lozano, A. Janda, A. Garcimartín, D. Maza, and I. Zuriguel, Flow and clogging in a silo with an obstacle above the orifice, Phys. Rev. E **86**, 031306 (2012).

[12] I. Zuriguel, D. R. Parisi, R. C. Hidalgo, C. Lozano, A. Janda, P. A. Gago, J. P. Peralta, L. M. Ferrer, L. A. Pugnaloni, E. Clément, D. Maza, I. Pagonabarraga, and A. Garcimartín, Clogging transition of many-particle systems flowing through bottlenecks, Sci. Rep. **4**, 7324 (2014).

[13] A. Johansson, D. Helbing, L. Buzna, and T. Werner, Self-organized pedestrian crowd dynamics: Experiments, simulations, and design solutions, Transport. Sci. **39**, 1 (2005).

[14] G. A. Frank and C. O. Dorso, Room evacuation in the presence of an obstacle, Physica A **390**, 2135 (2011).

[15] A. Garcimartín, J. M. Pastor, L. M. Ferrer, J. J. Ramos, C. Martín-Gómez, and I. Zuriguel, Flow and clogging of a sheep herd passing through a bottleneck, Phys. Rev. E **91**, 022808 (2015).

[16] T. Kawaguchi and T. Shimizu, Particle simulation of crowd evacuation, Safety Sci. Rev. **3**, 75 (2013), (in Japanese).

[17] C. Mankoc, A. Garcimartín, I. Zuriguel, D. Maza, and L. A. Pugnaloni, Role of vibrations in the jamming and unjamming of grains discharging from a silo, Phys. Rev. E **80**, 011309 (2009).

[18] C. C. Thomas and D. J. Durian, Fraction of Clogging Configurations Sampled by Granular Hopper Flow, Phys. Rev. Lett. **114**, 178001 (2015).

[19] A. Janda, I. Zuriguel, and D. Maza, Flow Rate of Particles Through Apertures Obtained from Self-Similar Density and Velocity Profiles, Phys. Rev. Lett. **108**, 248001 (2012).

[20] J. Choi, A. Kudrolli, R. R. Rosales, and M. Z. Bazant, Diffusion and Mixing in Gravity-Driven Dense Granular Flows, Phys. Rev. Lett. **92**, 174301 (2004).

[21] S. Moka and P. R. Nott, Statistics of Particle Velocities in Dense Granular Flows, Phys. Rev. Lett. **95**, 068003 (2005).

[22] A. V. Orpe and A. Kudrolli, Velocity Correlations in Dense Granular Flows Observed with Internal Imaging, Phys. Rev. Lett. **98**, 238001 (2007).

[23] C. C. Thomas and D. J. Durian, Intermittency and velocity fluctuations in hopper flows prone to clogging, Phys. Rev. E **94**, 022901 (2016).

[24] A. Ashour, S. Wegner, T. Trittel, T. Borzsonyi, and R. Stannarius, Outflow and clogging of shape-anisotropic grains in hoppers with small apertures, Soft Matter **13**, 402 (2017).

[25] H. Katsuragi, K. Anki-Reddy, and K. Endo (unpublished).

[26] N. V. Brilliantov, F. Spahn, J.-M. Hertzsch, and T. Pöschel, Model for collisions in granular gases, Phys. Rev. E **53**, 5382 (1996).

[27] L. E. Silbert, D. Ertas, G. S. Grest, T. C. Halsey, D. Levine, and S. J. Plimpton, Granular flow down an inclined plane: Bagnold scaling and rheology, Phys. Rev. E **64**, 051302 (2001).

[28] T. Schwager, V. Becker, and T. Pöschel, Coefficient of tangential restitution for viscoelastic spheres, Eur. Phys. J. E **27**, 107 (2008).

[29] V. Becker, T. Schwager, and T. Pöschel, Coefficient of tangential restitution for the linear dashpot model, Phys. Rev. E **77**, 011304 (2008).

[30] http://www.engineersedge.com/coeffients_of_friction.htm.

[31] T. Schwager and T. Pöschel, Coefficient of normal restitution of viscous particles and cooling rate of granular gases, Phys. Rev. E **57**, 650 (1998).

[32] S. Plimpton, Fast parallel algorithms for short-range molecular dynamics, J. Comput. Phys. **117**, 1 (1995).

[33] K. Endo and H. Katsuragi, Statistical properties of gravity-driven granular discharge flow under the influence of an obstacle, EPJ Web Conf. **140**, 03004 (2017).

[34] F. Alonso-Marroquin, S. I. Azeezullah, S. A. Galindo-Torres, and L. M. Olsen-Kettle, Bottlenecks in granular flow: When does an obstacle increase the flow rate in an hourglass? Phys. Rev. E **85**, 020301 (2012).

[35] A. Murray and F. Alonso-Marroquin, Increasing granular flow rate with obstructions, Pap. Phys. **8**, 080003 (2016).

[36] W. Losert, D. G. W. Cooper, J. Delour, A. Kudrolli, and J. P. Gollub, Velocity statistics in excited granular media, Chaos **9**, 682 (1999).

[37] F. Rouyer and N. Menon, Velocity Fluctuations in a Homogeneous 2D Granular Gas in Steady State, Phys. Rev. Lett. **85**, 3676 (2000).

[38] J. S. van Zon and F. C. MacKintosh, Velocity Distributions in Dissipative Granular Gases, Phys. Rev. Lett. **93**, 038001 (2004).

[39] N. Roussel, T. L. H. Nguyen, and P. Coussot, General Probabilistic Approach to the Filtration Process, Phys. Rev. Lett. **98**, 114502 (2007).

[40] J. Tang and R. P. Behringer, How granular materials jam in a hopper, Chaos **21**, 041107 (2011).

[41] F. Vivanco, S. Rica, and F. Melo, Dynamical arching in a two dimensional granular flow, Granular Matter **14**, 563 (2012).

[42] N. Iikawa, M. M. Bandi, and H. Katsuragi, Structural evolution of a granular pack under manual tapping, J. Phys. Soc. Jpn. **84**, 094401 (2015).

[43] N. Iikawa, M. M. Bandi, and H. Katsuragi, Sensitivity of Granular Force Chain Orientation to Disorder-Induced Metastable Relaxation, Phys. Rev. Lett. **116**, 128001 (2016).

[44] R. C. Hidalgo, C. Lozano, I. Zuriguel, and A. Garcimartín, Force analysis of clogging arches in a silo, Granular Matter **15**, 841 (2013).